10.1071/PVv2018n193p36

Wave equation imaging and adjoint-state inversion for micro-seismic monitoring

Ben Witten
bwitten@gmail.com

Ben Witten[1] and Jeffrey Shragge[2]

[1]*The University of Western Australia, School of Earth Sciences and School of Physics, Centre for Energy Geosciences, Perth Australia.*
[2]*Colorado School of Mines, Geophysics Department, Center for Wave Phenomena.*

Introduction

Human activities within the top few kilometres of the crust can induce significant changes in the Earth's stress field. Such activities include fluid injection for enhanced oil/gas recovery, wastewater disposal, CO_2 sequestration, or hydraulic fracturing purposes. Fluid injection can cause changes to the local and distal stress fields that may induce irreversible changes to the rock and cause earthquakes (Committee on Induced Seismicity Potential in Energy Technologies, 2013). One can monitor the Earth for the (micro-) seismic signals to detect potential earthquakes and, through data processing, estimate the earthquake location. The spatial and temporal distribution of the detected seismicity provides insight into how the injection is affecting the subsurface.

Understanding the distribution of earthquakes is crucial for a number of reasons, primarily hazard assessment and risk mitigation. Traditionally, seismic event studies have focused on naturally occurring, larger magnitude events, because these earthquakes present the most significant seismic hazard (Stein and Wysession, 1991). However, with the recent increase in fluid injection activities for hydraulic fracturing (or stimulation) and waste-water disposal, small events that are orders of magnitude weaker than those felt by humans have taken on an outsized importance (e.g. Rutledge and Phillips, 2003; Maxwell, 2010). Detecting and accurately locating these small events is critical for determining the efficiency and effectiveness of a fracture program – as well as the risks and potential hazards associated with subsurface fluid injection (e.g. Warpinski, 2013; British Columbia Oil and Gas Commission, 2016).

Producing accurate event locations, though, is largely a function of the signal strength and accurate knowledge of the subsurface velocity, both of which are often lacking during micro-seismic monitoring. Currently, there is no reliable established method for improving the velocity model from low signal-to-noise micro-seismic data. The primary objective of this article is to review a new method for improving subsurface velocity models using low signal-to-noise micro-seismic data that is able to produce accurate and reliable location estimates.

Herein, we review the cause of fluid-induced seismicity and how it is monitored by sensing arrays. We then briefly discuss current methods for locating the observed (micro-) seismic events and inverting the data for improved velocity models. These methods include standard earthquake seismology techniques that require picking arrivals on individual traces, and more recent techniques suitable for weak arrivals based on exploration seismology principles such as seismic migration and image-domain inversion. Finally, we summarise the new methodology and demonstrate its robustness to low signal-to-noise data with a case study from a hydraulic fracture data set in the Marcellus Shale, Ohio, USA.

Injection-related seismicity

Fluid-induced seismicity is driven by the injection of fluid into a subsurface geologic interval through boreholes, typically terminating between 1 and 3 km depth. The primary uses of fluid injection are long-term geologic storage of fluids, such as wastewater disposal and CO_2 sequestration (Elliston and Davis, 1944; Metz et al., 2005; Ferguson, 2015), as well as hydraulic fracturing (Economides and Nolte, 2000; Legarth et al., 2005). For sequestration, large volumes of fluid, often by-products of oil and gas extraction, are injected into suitable geologic reservoirs to mitigate potential environmental hazards. Hydraulic fracturing is also undertaken to improve permeability of a geologic interval for enhanced oil and gas extraction or geothermal production. The mechanism of fluid-induced seismicity is, fundamentally, the same in most instances: fluid injection increases the pore pressure leading to mechanical rock failure - an earthquake. The failure could be in the form of tensile breaking, shear displacement, or a combination thereof (Fischer and Guest, 2011). Hydraulic fracturing uses high-pressure injection with the intent of increasing the pore pressure beyond the minimum principal stress in the formation to cause tensile failure, thus inducing earthquakes as new fractures are formed (Hubbert and Willis, 1957). Fluid injection also induces shear displacements, which occur when pore pressure increases within a pre-existing fault causing a decrease in effective normal stress, either directly (McGarr et al., 2002; Zoback and Gorelick, 2012) or through pressure diffusion (Talwani and Acree, 1984; Shapiro et al., 2003). When the normal stress decreases beyond a critical point, an earthquake initiates as slip along the fault. For a more thorough discussion on reservoir geo-mechanics and fluid-induced seismicity see Zoback (2007) and Shapiro (2015).

When an earthquake occurs it releases energy in the form of seismic waves. The seismic waves are radiated outward as both compressional (P-) and shear (S-) waves, with the P-wave energy traveling at a faster speed than the S-wave energy. The energy is not released uniformly in space, but has a radiation pattern that depends on the failure mechanism and orientation, with P-wave amplitudes generally weaker than those of S-wave. The moment magnitude (M_w), or total energy released by an induced earthquake, is usually in the micro-seismic range (i.e.,

M_w < 4) and is not felt by humans. While most fluid induced earthquakes have $M_w < 0$, larger earthquakes on pre-existing faults have been induced by fluid injection [i.e. M_w = 5.7 and M_w = 5.3 in Oklahoma and Colorado, respectively (Keranen et al., 2013; Rubinstein et al., 2014)].

Seismic Monitoring

To monitor for potential fluid-induced seismicity, an array of seismometers or geophones is often deployed to measure the energy released as seismic waves as a function of ground motion. These devices can be placed in boreholes (e.g. Warpinski et al., 1998; Maxwell et al., 2010), at or near the surface (e.g. Duncan and Eisner, 2010; Pesicek et al., 2014), or a combination thereof (Eisner et al., 2010). Figure 1 shows a schematic diagram of an induced seismic monitoring program. In this diagram, the wellbore, shown in black, injects fluid in the subsurface, indicated by the dashed maroon lines. The fluid injection process may induce earthquakes nearby or at a distance through pressure diffusion, which is represented by the light red dashed arcs. The earthquakes, also called 'events', are shown as red 'explosions'. The red lines emanating from the near event represent seismic waves propagating from the source to the monitoring stations shown as triangles. In this case, there are both borehole and surface arrays, shown in blue and orange, respectively.

Borehole arrays have the dual advantage that they are usually located closer to the events and farther away from anthropogenic noise generated at the surface. Thus, they often record high signal-to-noise data and one can detect and process very weak events. Borehole monitoring, however, is limited by the number of suitable boreholes near the injection well, and therefore poor spatial coverage. Even where a suitable well is available the spatial distribution of the receivers is often poor, sometimes comprising only tens of sensors per well (e.g. Rutledge and Phillips, 2003; Maxwell et al., 2010). This limits the ability of the borehole arrays to record the full radiation pattern of an earthquake. When no suitable pre-existing borehole is available, the cost of drilling might be prohibitive for this type of monitoring.

Conversely, surface monitoring arrays have good spatial coverage with large channel counts, hundreds to thousands of sensors (e.g. Duncan and Eisner, 2010, Birkelo et al., 2012), and generally have the aperture to measure a much larger portion of the radiation pattern. Surface arrays often are comprised of relatively cheap sensors that are quick and easy to deploy, making them a cost effective monitoring solution. However, the drawback of surface arrays is the higher levels of noise and increased distance from the events, which lead to low signal-to-noise data (S/N < 1). Therefore, surface arrays usually do not detect events as weak as those measurable on borehole arrays.

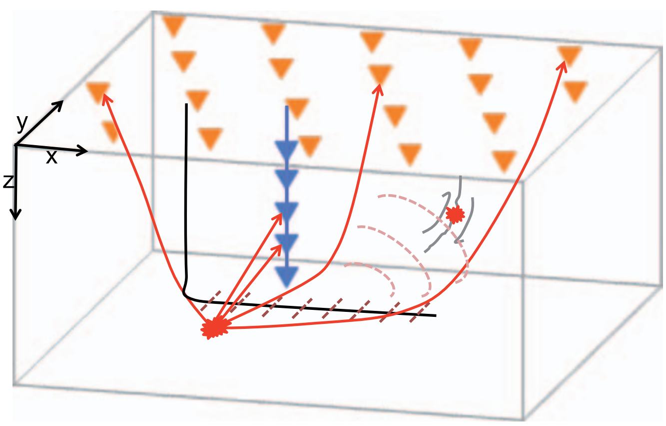

Figure 1. *Schematic diagram of fluid-induced seismicity with borehole and surface monitoring arrays. The black line is the injection well. The dashed maroon lines and dashed red arcs represent fluid injection and pressure diffusion, respectively. The red 'explosions' are earthquakes that emit seismic energy, shown as red arrows recorded at surface (orange) and borehole (blue) receivers.*

Figure 2 show data for strong (M_w = 0.24) and moderate (M_w = –0.47) micro-seismic events located more than 1.5 km below the surface. The data were recorded on a single three-component (3C) surface station, where the vertical component is shown in magenta and the two horizontal components are red and blue, respectively. For the strong event, the P- and S-wave first arrivals are clearly identifiable on the individual traces, while for the moderate event it is not possible to accurately identify the arrivals. Figure 3*a–c* and 3*d–f* show the complete 3C array data for the strong and moderate event, respectively. The data shown in Figure 2 are taken from trace 114 in this array. While it is possible to identify the events in the array data, picking accurate arrivals on each trace even in the strong example would be challenging.

Detected seismic arrivals can be used to produce estimates of the event properties such as location, magnitude and orientation. Of these, the event location is the most critical. Location estimates impact the determination of magnitude and orientation, and help evaluate the hydraulic fracture program by estimating both the lateral and vertical fracture growth and the complexity of the fracture network to optimise well completion (e.g. Maxwell, 2014). Additionally, the spatial and temporal distribution of events assists with estimating reservoir properties (e.g. Shapiro and Dinske, 2009), assessing potential hazards, and determining causality (i.e., natural vs induced seismicity) (Schoenball et al., 2015; Dempsey et al., 2016). This has implications for both effective completion operations and potential hazards from triggering a larger earthquake along the faults. Maxwell (2014) presents a more complete discussion on micro-seismic monitoring.

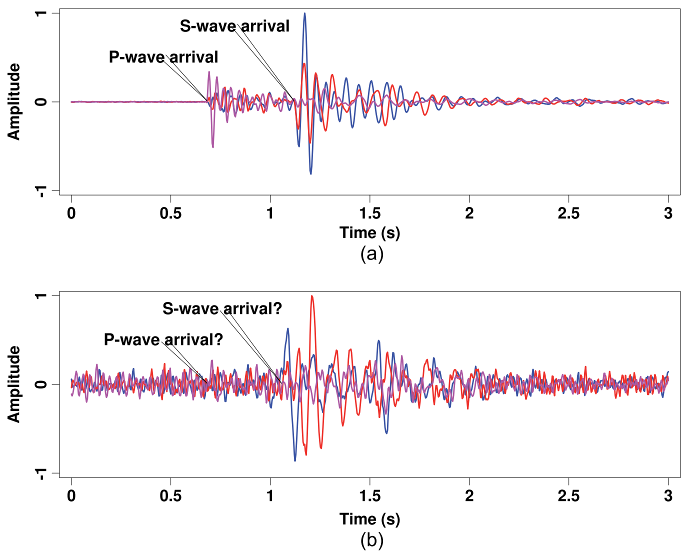

Figure 2. *Example of (a) strong, Mw=0.24, and (b) moderate, Mw=-0.47, micro-seismic arrivals recorded at a single surface station, normalized to respective maximum amplitude. The magenta trace is the vertical component, while the blue and red traces are the two horizontal components. Picked P- and S-wave arrivals are indicated.*

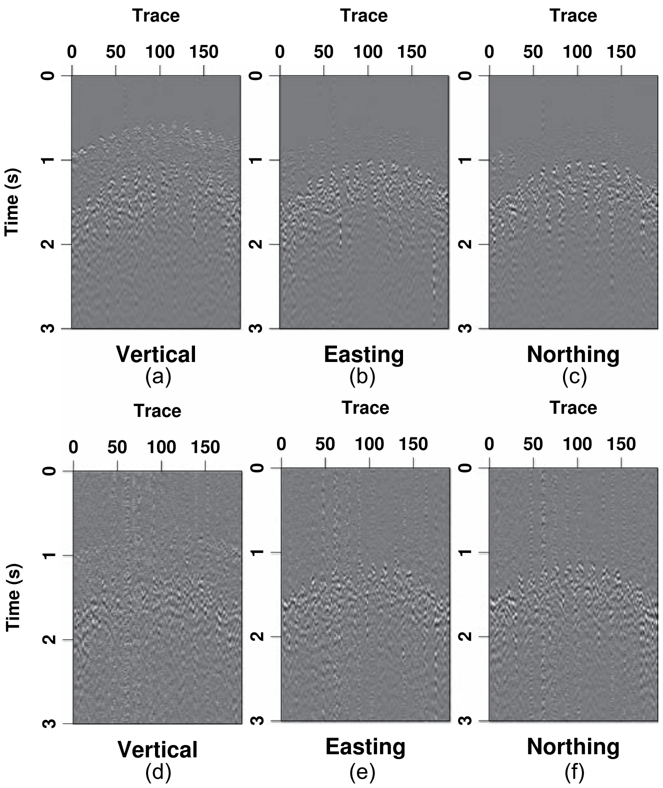

Figure 3. *Vertical, Northing, and Easting components for full surface array data from the strong (a–c) and moderate event (d–f) shown in Figure 2.*

Inaccurate location estimates can lead to incorrect conclusions about the causes and effects of induced seismicity. In late 2008, a few events were felt in the Dallas–Fort Worth (DFW), Texas area. This area is historically aseismic, which raised concerns that a nearby wastewater injection well could be inducing the earthquake events. This was concerning because of the potential hazard to the large population in the area and proximity to the DFW airport. Surface sensors were deployed to investigate whether the seismicity was natural or induced by the injection well. Reiter et al. (2012) and Janská and Eisner (2012) both examine this data set. Despite using the same data and similar location methods, the two studies locate the events at different depths, which appears to be largely driven by differing velocity models. Reiter et al. (2012) estimates that the events originate near the injection interval, while Janská and Eisner (2012) places them much deeper. This led to opposing conclusions as to whether the observed seismicity was natural or triggered. While further investigation determined the events were anthropologically induced (Frohlich et al., 2016), this clearly demonstrates that inaccurate location estimates caused by velocity model errors can lead to misinterpretation of subsurface processes and, in this case, the risk associated with the well and injection activities.

Earthquake location techniques

There are numerous ways to estimate earthquake event locations. Most techniques were developed to locate large earthquakes that produce high signal-to-noise data and generally require picking the P- and S-wave arrivals on individual traces, such as in Figure 2*a*. This process reduces the dataset from the full waveform to the pick times. Amongst the most straightforward ways to estimate the location is trilateration or the method of spheres (commonly known as triangulation). In this method, one estimates the distance from each receiver using the difference between the P- and S-wave arrival times and constant estimates of the P- and S-wave velocities (V_p and V_s). Using the distance estimates, we can draw spheres of equiprobable event locations. Doing this for at least three station locations yields an estimated source location where the spheres intersect. This method, while simple, assumes a homogeneous earth, which is obviously incorrect and may lead to imprecise (i.e., large region of intersection) and/or inaccurate (i.e., incorrect radius of spheres) location estimates.

To account for the heterogeneity of the earth, one can generate travel-time surfaces that conform to the variable velocity of the geology. These variable travel-time surfaces are usually created by tracing rays (Cerveny, 2000) from each cell in a P- and/or S-wave velocity model to create a travel-time surface between each model point and every receiver. Using the calculated synthetic travel times, it is common to implement grid search methods (e.g. Geiger, 1910; Buland, 1976; Sambridge and Kennett, 1986), which formulate the location estimation as an optimisation problem to find the grid cell with the minimum residual defined as the square of the difference between the calculated and observed travel times. The grid location with the minimal residual is the estimated earthquake location. While this is usually performed in a deterministic fashion, probabilistic extensions have been developed (Lomax et al., 2000; Husen et al., 2003). Grid search methods have been used to locate large events in many areas (e.g. Dreger et al., 1998; Richards-Dinger and Shearer, 2000).

Pick-based methods become infeasible when the signal-to-noise level of the data is too low to permit identification of individual arrivals, such as in Figure 2*b*. To handle low signal-to-noise data, methods using seismic migration principles have been developed for micro-seismic data (e.g. Kao and Shan, 2004; Artman et al., 2010). For earthquake monitoring data, migration creates an image of the source by refocusing the recorded waveform as a function of space. Figure 4 present the results of using a homogeneous Earth model to forward model 2D synthetic data as well as the resulting image created by applying migration to that data to refocus the event to the source location at $\mathbf{x_0}$=[x,z]=[2.8,1.5] km. There are two primary migration algorithms to generate this type of image: Kirchhoff and wave equation. Both techniques exploit the power of stacking recorded data across all traces to enhance the signal-to-noise ratio. Therefore, relative to pick-based methods, these approaches can be used to locate events from datasets exhibiting much lower signal-to-noise levels.

The Kirchhoff migration approach is similar to the grid search algorithm above, in the sense that travel times are computed

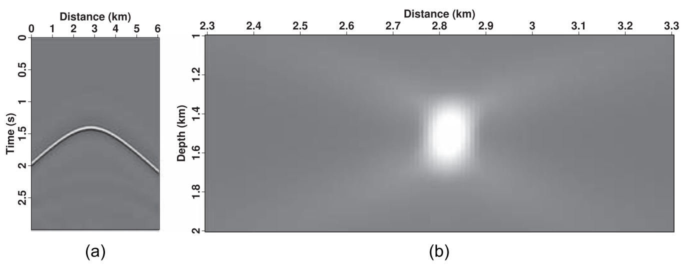

Figure 4. *Example 2D synthetic data (a) and resulting migrated image (b) with source location at $\mathbf{x_0}$= [2.8, 1.5] km. The migration algorithm refocuses the recorded energy in the migrated image. By using the correct velocity, the maximum in the image is at the true source location.*

from each grid cell to each receiver by ray tracing. However, rather than solving an optimisation problem, trace data are summed across the isochron (an equal time surface) generated from each grid cell for an assumed origin time, t_0, and stored for that location. Kirchhoff migration has been used successfully to locate micro-seismic events from low signal-to-noise micro-seismic data (e.g. Duncan and Eisner, 2010; Pesicek et al., 2014; Roux et al., 2014). This is also referred to as the back-projection method (Ishii et al., 2005) since it projects the data backward in time along the calculated rays. Given a *correct* velocity model and t_0 estimate, summing across the isochron from the cell containing the event location should optimally stack the arrivals to produce a maximized output. For all other grid locations at the same t_0 the isochrons will not perfectly coincide with the data and a lower amplitude output is produced. The grid cell with the maximum amplitude is the most likely source location for the given t_0. The assumed origin time is then shifted and the process repeated for all time samples in the recorded data. This method is computationally more expensive than pick-based methods and requires additional sensors, the appropriate number of which depends on the signal-to-noise level of the data. However, by stacking over an array of sensors and using the full wavefield, it can locate events using data with much lower signal-to-noise levels than the methods discussed above.

The second class of migration algorithms is wave-equation migration, also called back-propagation, which numerically propagates recorded data backwards in time through a velocity model to reconstruct the source wavefields. This can be done with either time- or frequency-domain propagators. Given a suitably accurate velocity model, the recorded energy will maximally constructively interfere at the source location, $\mathbf{x_0}$, and t_0. Figure 5 shows example reconstructed P- and S-wavefield snapshots at different propagation times. The left (right) panels are the P-wave (S-wave) snapshots. The upper panels are when $t>t_0$, the middle panels are at $t=t_0$, and the lower panels for $t<t_0$. Once the wavefields have propagated through the source location, they defocus and are no longer representative of the true wavefield since we would need to remove the energy at the source location due to causality arguments. We see here that both the P- and S-wavefields collapse and focus at the source location ($\mathbf{x_0}$ = [2.8,1.5] km) and at t_0 as they both originate at the same spatial and temporal point. One could scan through snapshots to identify the location and time of maximum focus as recognized by McMechan (1982). To eliminate the time-consuming 3D scanning process, one can apply a zero-lag imaging condition that stacks over the time coordinate to produce an image solely as function of space (e.g. Figure 4*b*). Correlation-based imaging conditions are similar to those used in reflection seismic migration (Claerbout, 1971). These imaging conditions correlate various modes of the source wavefield, such as auto- and cross-correlation of P- and S-wavefield energy (Artman et al., 2010). The P-P and S-S autocorrelation imaging conditions are:

$$I_{pp}(\boldsymbol{x}) = \int_T^0 u_p(\boldsymbol{x},t)u_p(\boldsymbol{x},t)dt, (1)$$

$$I_{ss}(\boldsymbol{x}) = \int_T^0 u_s(\boldsymbol{x},t)u_s(\boldsymbol{x},t)dt, (2)$$

and the P-S cross-correlation imaging condition is expressed as:

$$I_{ps}(\boldsymbol{x}) = \int_T^0 u_p(\boldsymbol{x},t)u_s(\boldsymbol{x},t)dt, (3)$$

where I_{ij} are the images, and u_p and u_s are the reconstructed P- and S-wavefields, respectively.

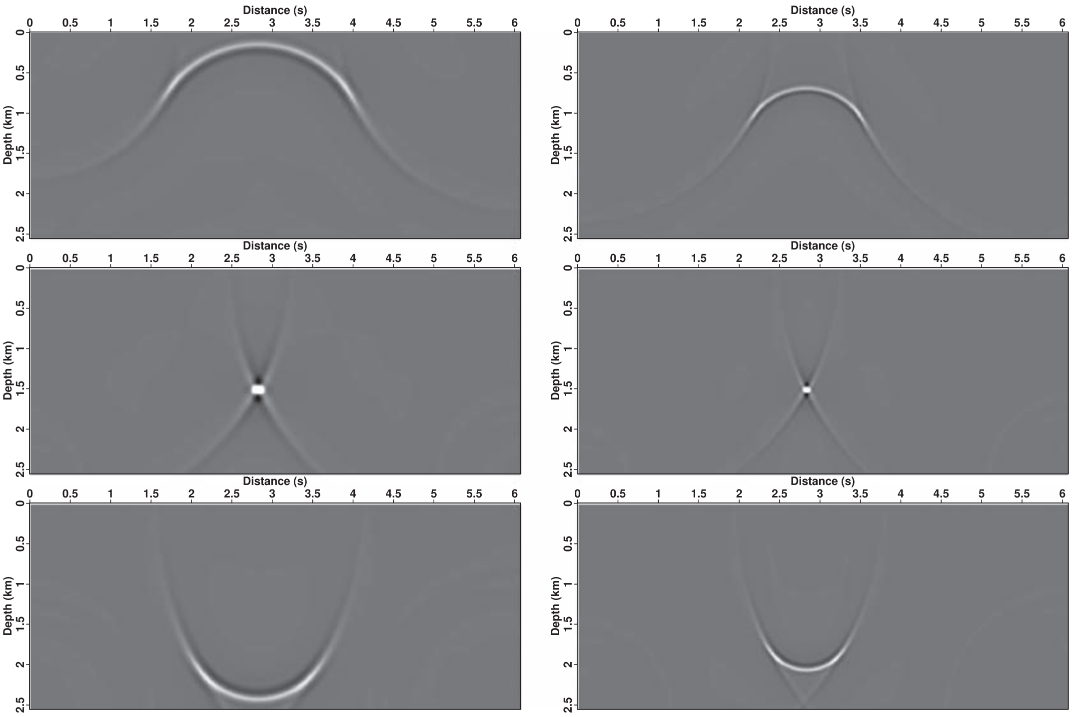

Figure 5. *Snapshots reconstructed P- and S-wavefields (left and right columns, respectively) using wave-equation migration. Top panels are after source initiation ($t > t_0$), middle panels are at source initiation time ($t = t_0$), and bottom panels are prior to source initiation ($t < t_0$).*

Similar to Kirchhoff methods, wave-equation migration can locate events in low signal-to-noise data by effectively stacking the recorded waveforms. In contrast to Kirchhoff migration, it more accurately replicates wave propagation physics through a more physically accurate (i.e., non-asymptotic) form of the wave equation that may account for particle motion, anisotropy, multi-pathing, etc. The principle drawback of this technique is that it is more computationally expensive than any of the methods described above.

All the location methods described thus far are sensitive to the inputs. The inputs are pick or trace data for the pick-based and migration methods, respectively, and a velocity model. Provided accurate input, both types of methods produce accurate locations. However, when the signal-to-noise level of individual traces becomes too low to pick with confidence, location estimates from pick-based methods become inaccurate (e.g. Pavlis, 1986; Billings et al., 1994). For migration-based methods, the signal-to-noise can be substantially lower, though there are still limits based on noise characteristics and acquisition geometry (Cieslik et al., 2016). All event location methods rely on an accurate velocity model to produce accurate locations (e.g. Gajewski and Tessmer, 2005; Eisner et al., 2009). Relative approaches, such as the double-difference method (Waldhauser and Ellsworth, 2000), try to account for velocity error to provide relative locations. However, even these methods are similarly sensitive to velocity model error (Michelini and Lomax, 2004). Therefore, constructing an accurate velocity model is essential to produce reliable location estimates.

Velocity inversion techniques

Velocity updating for earthquake data is most commonly done through travel-time tomography (TTT) (e.g. Aki and Lee, 1976; Thurber, 1983; Rawlinson and Sambridge, 2003). TTT attempts to produce a velocity model that minimizes differences between ray-traced travel times for all source-receiver pairs and picked arrivals. In micro-seismic monitoring, this has been used when source locations and origin times are known, such as perforation and calibration shots recorded in a borehole (Warpinski et al., 2003; Bardainne and Gaucher, 2010). However, for scenarios where source locations and onset times are unknown, as is the case with (micro-seismic) earthquakes, it is preferable to jointly update the source location and velocity model (Thurber, 1992) since the original location estimate may be incorrect due to velocity model error. This method has been successfully applied to events detected during borehole micro-seismic monitoring (Grechka and Yaskevich, 2014; Chen et al., 2017). Like pick-based location algorithms, this method is limited by the requirement of picking arrivals on individual traces and, therefore, may not be suitable for surface micro-seismic monitoring.

Another class of velocity updating methods uses the entire waveform through adjoint-state tomography. Adjoint-state tomography forms velocity updates by correlating 'state variables' with 'adjoint-state variables'. In seismic monitoring scenarios, the state variables are wavefields generated by back-propagating the recorded data, and the adjoint-state variables are the forward-propagated 'adjoint sources' derived from residuals defined as the mismatch between the expected and current estimate of the input (e.g. trace data or image). There are two primary classes of geophysical adjoint-state tomography that are distinguished by the domain where the residuals are calculated. The first are data-domain methods, such as full waveform inversion (FWI) (Lailly, 1983; Tarantola, 1984; Fichtner et al., 2006), where one attempts to match forward-modelled synthetic data to the recorded trace data. The second are image-domain techniques, like differential semblance optimisation (DSO) (Symes and Carazzone, 1991; Symes, 1993; Shen, 2008), which attempt to optimally focus images.

FWI is similar to TTT in the sense that synthetic data are generated and compared to observations. However, FWI uses wave-equation propagation to forward model the data, and the residuals are usually computed as the difference between the modelled and recorded traces, rather than ray tracing and picked arrival times. This precludes a need for picking and can produce high-resolution velocity models. While FWI has been used to produce velocity models for large-magnitude earthquake data (e.g. Tape et al., 2009; Kamei et al., 2012), it has not been applied on field micro-seismic data. This is due to the associated computational complexity, the requirements of a very accurate starting velocity model, origin time t_0, and source location estimate $\mathbf{x_0}$, and low signal-to-noise levels of recorded micro-seismic data. If the data exhibit an insufficient signal-to-noise ratio the FWI algorithm will fit the noise rather than signal, leading to poor convergence and inaccurate interpretation. Thus, FWI is largely impractical for surface micro-seismic monitoring.

In contrast to the velocity updating techniques above, DSO does not attempt to directly match the input data; rather, it optimises the foci of migrated images. DSO has primarily been used to improve images of subsurface structure either through controlled source reflection experiments (e.g. Mulder and ten Kroode, 2002; Albertin et al., 2006; Shen and Symes, 2008) or converted waves from earthquake data (Shabelansky et al., 2015). The quality of the migrated image is assessed by extending the correlation beyond zero lag. For this imaging case, the extended P-S image of equation 3 is

$$I_{ps}(\boldsymbol{x},\boldsymbol{\lambda},\tau) = \int_T^0 u_p(\boldsymbol{x}-\boldsymbol{\lambda},t-\tau)u_s(\boldsymbol{x}+\boldsymbol{\lambda},t+\tau)dt, (4)$$

where λ and τ are spatial and temporal shifts, respectively. Since the P- and S-wavefields both originate at the same point in space and time, the image should be maximal at the source location and at zero lag in space and time (i.e., $\lambda = 0$ m and $\tau = 0$ s). An image having a maximum at $\lambda \neq 0$ m and/or $\tau \neq 0$ s indicates velocity error (Witten and Shragge, 2015). Residuals are defined by applying a penalty function to the extended image, which removes energy around zero lag. While DSO cannot achieve the resolution of FWI, it has a less stringent requirement on the initial model, making it applicable to locations where little *a priori* information is known. Since the residuals for DSO are defined in the image domain it is potentially suitable for producing reliable velocity updates for surface micro-seismic data.

In addition to the extended image (equation 4), the velocity model can be assessed by examining the suite of zero-lag images (equations 1-3). Since the P- and S-waves for a given event originate at the same point in the earth, all images should have maxima at the same model location. If the images are inconsistent this is an additional indication of P- and/or S-wave velocity error. Witten and Shragge (2017*a*) present an adjoint-state inversion methodology that exploits the expected consistency amongst the suite of zero-lag and extended images that is robust to low signal-to-noise data and common micro-seismic acquisition geometries.

Field data example

Figure 6 shows the acquisition geometry of a surface monitoring data set collected over a multi-well hydraulic fracture job in the Marcellus Shale, Ohio, USA. The red dots show the surface location of 192 3C geophones covering an area of approximately 6.5 x 6.0 km^2. The white box indicates the approximate extent of the horizontal injection wells. The hydraulic stimulation consisted of multiple wells, and more than 100 stages were completed that targeted the Marcellus Shale Formation (MSF), a thin organic rich interval located at approximately 1.75 km below the surface (1.5 km below mean sea level). The MSF is bounded directly below by a thick limestone layer, which has been shown to form a barrier for fracture growth.

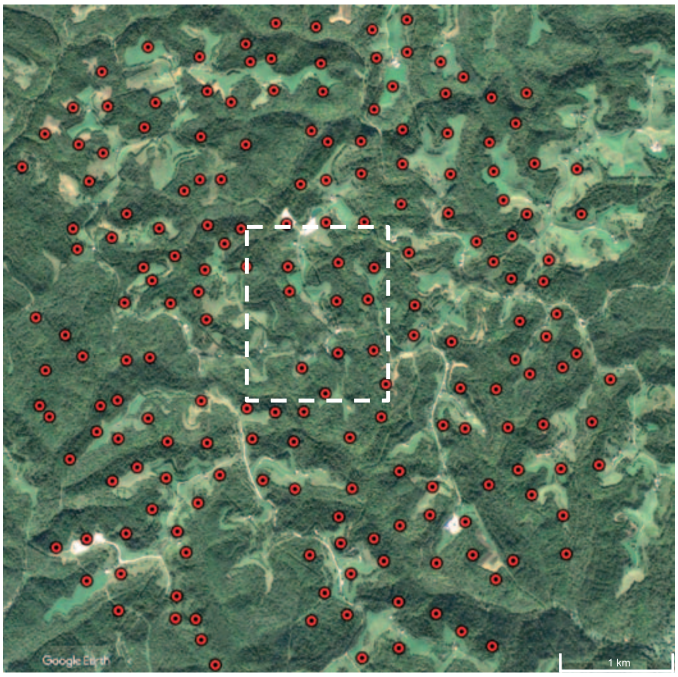

Figure 6. *Satellite image showing topography with geophone locations in red. The white box (1.5 x 1.25 km^2) indicates the approximate stimulated volume (from Witten and Shragge, 2017b).*

The initial velocity information is taken from a single dipole sonic log acquired at the well head. The P- and S-wave velocities are measured from below the reservoir almost up to the surface. The well-log data were smoothed and extrapolated into a 3D volume, accounting for known minor regional structural dip of approximately 2%. The background of Figure 7 shows the initial velocity model. Each face of the flattened cube shows a slice extracted through the 3D volume in the X1–X2 plane (top face), X2–Z plane (front face), and X1–Z plane (side face). The crosshairs on the panels indicate the extraction locations for each face. In this case, the faces shown are the following planes: Z = 1.53 km, X1 = 3.22 km, and X2 = 2.93 km. For reference, we project approximate boundaries of the stimulated volume on the 2D faces as dashed white boxes. The region of low V_P/V_S values is the reservoir interval.

A catalog of over 10,000 detected events was provided by the operator, from which we selected 28 events for inversion and another 100 events for validating the inversion results. The 100 validation events vary in magnitude from Mw = –1.14 to Mw = –0.18. For a full discussion on the methodology and results see Witten and Shragge (2017*b*). The symbols on Figure

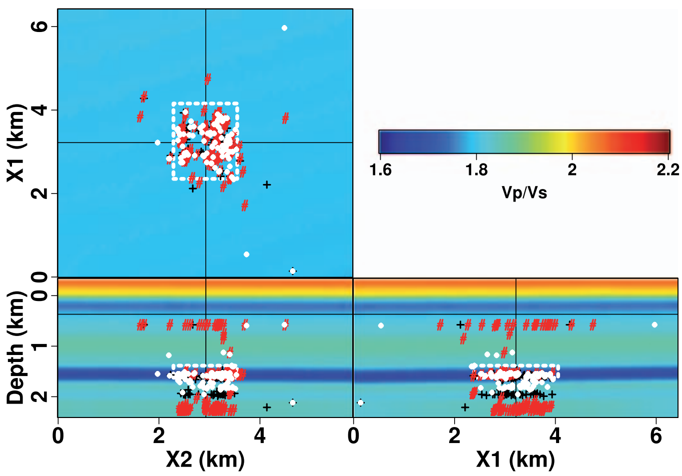

Figure 7. *Initial Vp/Vs model and 100 estimated event locations. The black '+', red '#', and white 'o' indicate the PP, SS, and PS event location estimates. The dashed white boxes indicate the approximate stimulated volume.*

7 are the estimated event location of the 100 validation events using the initial imaging velocity model. The black '+' are the PP image locations (equation 1), the red '#' are the SS image locations (equation 2), and the white 'o' are the PS image locations (equation 3). We note that there are large discrepancies between the location estimates between the various imaging conditions. In particular, the SS locations are often either much too deep or shallow, while the PP ones are deeper than expected. Due to the underlying limestone formation mentioned above, it is unlikely that the events originate in this unit.

Figure 8 shows the PP, SS, zero-lag PS, and an extraction from the extended PS volume, respectively. The input data are the event traces shown in Figure 3*d–f*, which are migrated through the initial velocity model. We see a clear discrepancy between focal locations of the zero-lag images, particularly the SS image and a slight shift from, and lack of symmetry about, zero-lag in the extended image volume. This indicates velocity error and provides image-domain residual for the inversion procedure.

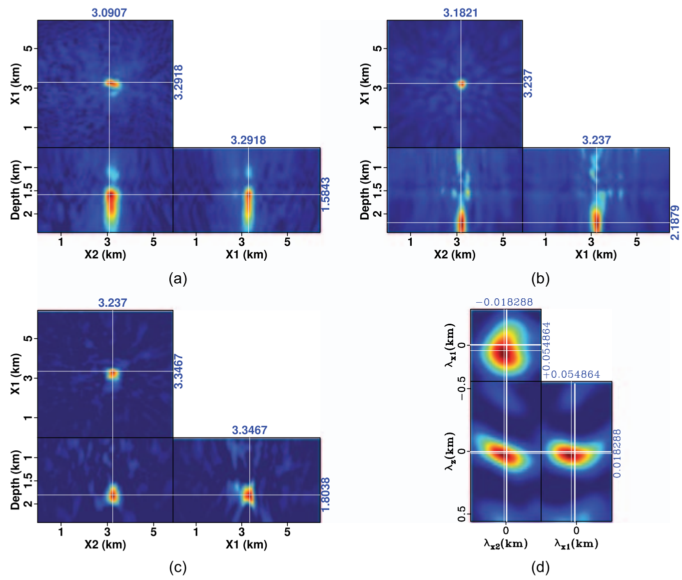

Figure 8. *Image volumes using the initial velocity model data of the moderate event shown in Figure 3d–f. Panels a–c are the zero-lag PP, SS, and PS images. Panel d shows a slice through the extended PS image volume extracted at the maximum location of the zero-lag image (from Witten and Shragge, 2017b).*

Using images such as those in Figure 8, we invert for P- and S-wave velocity models that optimally focus the suite of images without picking any event arrivals. Figure 9 shows the inverted V_P/V_S. Again, the symbols (black '+', red '#', and white 'o') indicate the estimated PP, SS, and PS event locations for the 100 validation events. Comparing the event locations in Figure 9 to those in Figure 7, we note that the inverted velocity model produces much more self-consistent event locations with many fewer situated beneath the reservoir interval. Figure 10 shows the same event as Figure 8 for the zero-lag PP, SS, and PS images, and an extraction from the extended PS volume, respectively, using the inverted velocity model. Again, we note much better focal location self-consistency among the zero-lag images and a more symmetric focus around zero lag in the extended image.

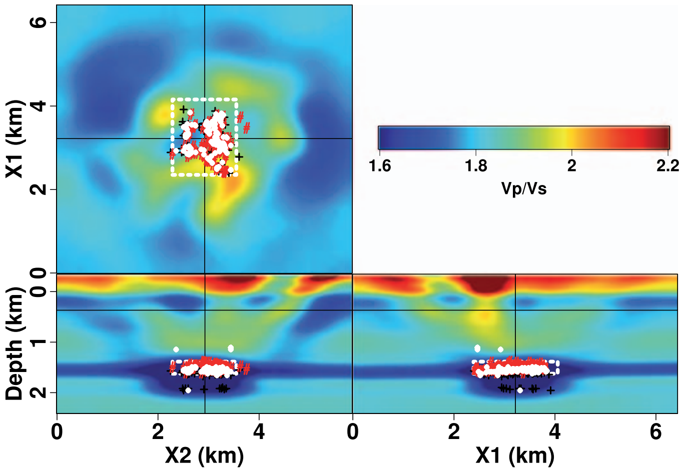

Figure 9. *Final inverted Vp/Vs model and 100 estimated event locations. The black '+', red '#', and white 'o' indicate the PP, SS, and PS event location estimates. The dashed white boxes indicate the approximate stimulated volume.*

Discussion and conclusions

While the results shown in Figure 9 do not depict an accurate representation of the geology, they do provide a suitable imaging velocity. Unlike in the conventional exploration seismic context, the goal in micro-seismic monitoring is not to make interpretations about the geological structure of the earth; rather, it is to determine the location and potential causality of detected earthquakes to assess oil and gas production efficiency and mitigate potential hazards. Therefore, the obtained inversion results provide the optimal solution for imaging. The main drawback of the image-domain inversion methodology presented is the computational expense. However, as shown a limited number of events are needed for the inversion and with modern computation hardware, particularly graphics processing units (GPUs), the results can be obtained in a reasonable time frame. The principal benefit of this technique is that it provides a viable means to invert for the elastic velocity model to optimally image the detected events without the need for picking arrivals. This is particularly important for surface micro-seismic monitoring where the detected events are often too weak to be seen on individual traces. Therefore, the image domain technique provides the only known means to accurately update the model in these scenarios.

As injection programs are becoming increasingly common, it will be more important to monitor for subsurface changes to ensure the social license to operate, guarantee safe operations

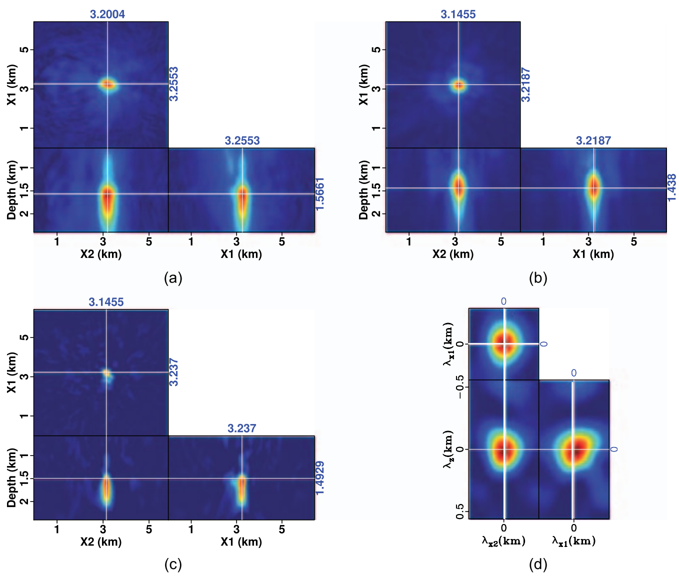

Figure 10. *Zero-lag image volumes (a) PP, (b) SS, and (c) PS using the inverted velocity model and data of the moderate event shown in Figure 3d–f and (d) shows a slice through the extended PS image volume extracted at the maximum location of the zero-lag image (from Witten and Shragge, 2017b).*

or, perhaps, to meet regulatory requirements. Given that the monitoring will often be surface-based to help minimise costs, the method may be optimal to produce the most accurate location estimates and therefore reliable interpretations of the subsurface changes resulting from the injection.

Acknowledgements

We thank Statoil USA for providing the Marcellus dataset and allowing publication of the results. Ben Witten acknowledges funding by an Australian Government Research Training Program Scholarship. We especially thank the Australian Society of Exploration Geophysics Research Foundation (ASEGRF) for providing a grant that supported the research, development, and application of the work described herein.

References

Aki, K., and Lee, W. H. K., 1976, Determination of three dimensional velocity anomalies under a seismic array using P-arrival times from local earthquakes: part I-a homogeneous initial model: *Journal of Geophysical Research*, **81**, 4381–4399. doi:10.1029/JB081i023p04381

Albertin, U., Sava, P., Etgen, J., and Maharramov, M., 2006, Adjoint wave-equation velocity analysis: 76th Annual International Meeting, SEG Technical Program Expanded Abstracts, SEG, 3345–3349.

Artman, B., Podladtchikov, I., and Witten, B., 2010, Source location using time-reverse imaging: *Geophysical Prospecting*, **58**(5), 861–873. doi:10.1111/j.1365-2478.2010.00911.x

Bardainne, T., and Gaucher, E., 2010, Constrained tomography of realistic velocity models in microseismic monitoring using calibration shots: *Geophysical Prospecting*, **58**(5), 739–753. doi:10.1111/j.1365-2478.2010.00912.x

Billings, S. D., Sambridge, M. S., and Kennett, B. L. N., 1994, Errors in hypocenter location: picking, model, and magnitude dependence: *Bulletin of the Seismological Society of America*, **84**(6), 1978–1990.

Birkelo, B., Cieslik, K., Witten, B., Montgomery, S., Artman, B., Miller, D., and Norton, M., 2012, High quality surface microseismic data illuminates fracture treatments: a case study in the Montney: *The Leading Edge*, **31**(11), 1318–1325. doi:10.1190/tle31111318.1

British Columbia Oil and Gas Commission, 2016, *Ground Motion monitoring and submission guideline*: https://www.bcogc.ca/ground-motion-monitoring-and-submission-guideline (accessed 13 March 2017).

Buland, R., 1976, The mechanics of locating earthquakes: *Bulletin of the Seismological Society of America*, **66**(1), 173–187.

Cerveny, V., 2000, *Seismic ray method*: Cambridge University Press.

Chen, Y., Zhang, H., Miao, Y., Zhang, Y., and Liu, Q., 2017, Back azimuth constrained double-difference seismic location and tomography for downhole microseismic monitoring: *Physics of the Earth and Planetary Interiors*, **264**, 35–46. doi:10.1016/j.pepi.2016.10.003

Cieslik, K., Artman, B., Roche, S., and Gumble, J., 2016, Signal to noise analysis of densely sampled microseismic data: Presented at the AAPG/SEG International Conference & Exhibition.

Claerbout, J., 1971, Toward a unified theory of reflector mapping: *Geophysics*, **36**, 467–481. doi:10.1190/1.1440185

Committee on Induced Seismicity Potential in Energy Technologies, 2013, *Induced seismicity potential in energy technologies*: National Academies Press.

Dempsey, D., Suckale, J., and Huang, Y., 2016, Collective properties of injection-induced earthquake sequences: 2. Spatiotemporal evolution and magnitude frequency distributions: *Journal of Geophysical Research. Solid Earth*, **121**(5), 3638–3665. doi:10.1002/2015JB012551

Dreger, D., Uhrhammer, R., Pasyanos, M., Franck, J., and Romanowicz, B., 1998, Regional and far-regional earthquake locations and source parameters using sparse broadband networks: a test on the Ridgecrest sequence: *Bulletin of the Seismological Society of America*, **88**(6), 1353–1362.

Duncan, P. M., and Eisner, L., 2010, Reservoir characterization using surface microseismic monitoring: *Geophysics*, **75**(5), A139–A146. doi:10.1190/1.3467760

Economides, M. J., and K. G. Nolte, 2000, *Reservoir stimulation*: Wiley: New York.

Eisner, L., Duncan, P. M., Heigl, W. M., and Keller, W. R., 2009, Uncertainties in passive seismic monitoring: *The Leading Edge*, **28**(6), 648–655. doi:10.1190/1.3148403

Eisner, L., Hulsey, B. J., Duncan, P., Jurick, D., Werner, H., and Keller, W., 2010, Comparison of surface and borehole locations of induced seismicity: *Geophysical Prospecting*, **58**(5), 809–820. doi:10.1111/j.1365-2478.2010.00867.x

Elliston, H., and Davis, W., 1944, A method of handling salt-water disposal, including treatment of water: drilling and production practice, American Petroleum Institute, API-44-122.

Ferguson, G., 2015, Deep injection of waste water in the Western Canada Sedimentary Basin: *Ground Water*, **53**(2), 187–194. doi:10.1111/gwat.12198

Fichtner, A., Bunge, H.-P., and Igel, H., 2006, The adjoint method in seismology: I. Theory: *Physics of the Earth and Planetary Interiors*, **157**(1–2), 86–104. doi:10.1016/j.pepi.2006.03.016

Fischer, T., and Guest, A., 2011, Shear and tensile earthquakes caused by fluid injection: *Geophysical Research Letters*, **38**(5). doi:10.1029/2010GL045447

Frohlich, C., DeShon, H., Stump, B., Hayward, C., Hornbach, M., and Walter, J. I., 2016, A historical review of induced earthquakes in Texas: *Seismological Research Letters*, **87**, 1022–1038. doi:10.1785/0220160016

Gajewski, D., and Tessmer, E., 2005, Reverse modelling for seismic event characterization: *Geophysical Journal International*, **163**(1), 276–284. doi:10.1111/j.1365-246X.2005.02732.x

Geiger, L., 1910, Herdbestimmung bei erdbeben aus den ankunftszeiten: Nachrichten von der Gesellschaft der Wissenschaften zu Göttingen: *Mathematisch-Physikalische Klasse*, **1910**, 331–349.

Grechka, V., and Yaskevich, S., 2014, Azimuthal anisotropy in microseismic monitoring: a Bakken case study: *Geophysics*, **79**(1), KS1–KS12. doi:10.1190/geo2013-0211.1

Hubbert, M. K., and Willis, D. G., 1957, Mechanics of hydraulic fracturing: *Journal of Petroleum Technology*, **IX**(6), 153–166.

Husen, S., Kissling, E., Deichmann, N., Wiemer, S., Giardini, D., and Baer, M., 2003, Probabilistic earthquake location in complex three-dimensional velocity models: application to Switzerland: *Journal of Geophysical Research. Solid Earth*, **108**(no. B2).

Ishii, M., Shearer, P. M., Houston, H., and Vidale, J. E., 2005, Extent, duration and speed of the 2004 Sumatra-Andaman earthquake imaged by the Hi-Net array: *Nature*, **435**(7044), 933–936. doi:10.1038/nature03675

Janská, E., and Eisner, L., 2012, Ongoing seismicity in the Dallas–Fort Worth area: *The Leading Edge*, **31**(12), 1462–1468. doi:10.1190/tle31121462.1

Kamei, R., Pratt, R. G., and Tsuji, T., 2012, Waveform tomography imaging of a megasplay fault system in the seismogenic Nankai subduction zone: *Earth and Planetary Science Letters*, **317–318**, 343–353. doi:10.1016/j.epsl.2011.10.042

Kao, H., and Shan, S.-J., 2004, The source-scanning algorithm: mapping the distribution of seismic sources in time and space: *Geophysical Journal International*, **157**(2), 589–594. doi:10.1111/j.1365-246X.2004.02276.x

Keranen, K. M., Savage, H. M., Abers, G. A., and Cochran, E. S., 2013, Potentially induced earthquakes in Oklahoma, USA: links between wastewater injection and the 2011 Mw 5.7 earthquake sequence: *Geology*, **41**(6), 699–702. doi:10.1130/G34045.1

Lailly, P., 1983, The seismic inverse problem as a sequence of before stack migration: Conference on Inverse Scattering, Theory and Application, Society of Industrial and Applied Mathematics, Expanded Abstracts, 206-220.

Legarth, B., Huenges, E., and Zimmermann, G., 2005, Hydraulic fracturing in a sedimentary geothermal reservoir: results and implications: *International Journal of Rock Mechanics and Mining Sciences*, **42**(7–8), 1028–1041. doi:10.1016/j.ijrmms.2005.05.014

Lomax, A., Virieux, J., Volant, P., and Berge-Thierry, C., 2000, *Probabilistic earthquake location in 3D and layered models: advances in seismic event location*, Springer: The Netherlands, 101–134.

Maxwell, S., 2010, Microseismic: growth born from success: *The Leading Edge*, **29**(3), 338–343. doi:10.1190/1.3353732

Maxwell, S., 2014, Microseismic imaging of hydraulic fracturing: improved engineering of unconventional reservoirs: Canadian Society of Exploration Geophysicists.

Maxwell, S., Rutledge, J., Jones, R., and Fehler, M., 2010, Petroleum reservoir characterization using downhole microseismic monitoring: *Geophysics*, **75**(5), A129–A137. doi:10.1190/1.3477966

McGarr, A., Simpson, D., and Seeber, L., 2002, Case histories of induced and triggered seismicity, in *International Handbook of Earthquake and Engineering Seismology, Part A*: Academic Press, *International Geophysics*, 81, 647–661.

McMechan, G. A., 1982, Determination of source parameters by wavefield extrapolation: *Geophysical Journal International*, **71**(3), 613–628. doi:10.1111/j.1365-246X.1982.tb02788.x

Metz, B., Davidson, O., De Coninck, H., Loos, M., and Meyer, L., 2005, IPCC special report on carbon dioxide capture and storage: technical report, Intergovernmental Panel on Climate Change, Geneva (Switzerland). Working Group III.

Michelini, A., and Lomax, A., 2004, The effect of velocity structure errors on double-difference earthquake location: *Geophysical Research Letters*, **31**, L09602.

Mulder, W., and ten Kroode, A., 2002, Automatic velocity analysis by differential semblance optimization: *Geophysics*, **67**(4), 1184–1191. doi:10.1190/1.1500380

Pavlis, G. L., 1986, Appraising earthquake hypocenter location errors: a complete, practical approach for single-event locations: *Bulletin of the Seismological Society of America*, **76**(6), 1699–1717.

Pesicek, J. D., Child, D., Artman, B., and Cieślik, K., 2014, Picking versus stacking in a modern microearthquake location: comparison of results from a surface passive seismic monitoring array in Oklahoma: *Geophysics*, **79**(6), KS61–KS68. doi:10.1190/geo2013-0404.1

Rawlinson, N., and Sambridge, M., 2003, Seismic traveltime tomography of the crust and lithosphere: *Advances in Geophysics*, **46**, 81–198. doi:10.1016/S0065-2687(03)46002-0

Reiter, D., Leidig, M., Yoo, S.-H., and Mayeda, K., 2012, Source characteristics of seismicity associated with underground wastewater disposal: a case study from the 2008 Dallas-Fort Worth earthquake sequence: *The Leading Edge*, **31**(12), 1454–1460. doi:10.1190/tle31121454.1

Richards-Dinger, K. B., and Shearer, P. M., 2000, Earthquake locations in southern California obtained using source-specific station terms: *Journal of Geophysical Research. Solid Earth*, **105**(no. B5), 10939–10960. doi:10.1029/2000JB900014

Roux, P.-F., Kostadinovic, J., Bardainne, T., Rebel, E., Chmiel, M., Van Parys, M., Macault, R., and Pignot, L., 2014, Increasing the accuracy of microseismic monitoring using surface patch arrays and a novel processing approach: *First Break*, **32**(7), 95–101.

Rubinstein, J. L., Ellsworth, W. L., McGarr, A., and Benz, H. M., 2014, The 2001-present induced earthquake sequence in the Raton Basin of northern New Mexico and southern Colorado: *Bulletin of the Seismological Society of America*, **104**, 2162–2181. doi:10.1785/0120140009

Rutledge, J. T., and Phillips, W. S., 2003, Hydraulic stimulation of natural fractures as revealed by induced microearthquakes, Carthage Cotton Valley gas field, east Texas: *Geophysics*, **68**(2), 441–452. doi:10.1190/1.1567214

Sambridge, M. S., and Kennett, B. L. N., 1986, A novel method of hypocentre location: *Geophysical Journal International*, **87**(2), 679. doi:10.1111/j.1365-246X.1986.tb06644.x

Schoenball, M., Davatzes, N. C., and Glen, J. M. G., 2015, Differentiating induced and natural seismicity using space-time-magnitude statistics applied to the Coso Geothermal field: *Geophysical Research Letters*, 42(15), 6221–6228.

Shabelansky, A. H., Malcolm, A. E., Fehler, M. C., Shang, X., and Rodi, W. L., 2015, Source-independent full wavefield converted-phase elastic migration velocity analysis: *Geophysical Journal International*, **200**(2), 952–966. doi:10.1093/gji/ggu450

Shapiro, S., 2015, *Fluid-induced seismicity*: Cambridge University Press.

Shapiro, S., and Dinske, C., 2009, Fluid-induced seismicity: pressure diffusion and hydraulic fracturing: *Geophysical Prospecting*, **57**(2), 301–310. doi:10.1111/j.1365-2478.2008.00770.x

Shapiro, S. A., Patzig, R., Rothert, E., and Rindschwentner, J., 2003, Triggering of seismicity by pore-pressure perturbations: permeability-related signatures of the phenomenon: *Pure and Applied Geophysics*, **160**(5), 1051–1066. doi:10.1007/PL00012560

Shen, P. 2008, Wave equation migration velocity analysis by differential semblance optimization: PhD thesis, Rice University, Houston, TX.

Shen, P., and Symes, W., 2008, Automatic velocity analysis via shot profile migration: *Geophysics*, **73**(5), VE49–VE59. doi:10.1190/1.2972021

Stein, S., and Wysession, M., 1991, An introduction to seismology, earthquakes, and Earth structure: Wiley.

Symes, W., 1993, A differential semblance criterion for inversion of multioffset seismic reflection data: *Journal of Geophysical Research. Solid Earth*, **98**(no. B2), 2061–2073. doi:10.1029/92JB01304

Symes, W., and Carazzone, J., 1991, Velocity inversion by differential semblance optimization: *Geophysics*, **56**(5), 654–663. doi:10.1190/1.1443082

Talwani, P., and Acree, S., 1984, Pore pressure diffusion and the mechanism of reservoir-induced seismicity: *Pure and Applied Geophysics*, **122**(6), 947–965. doi:10.1007/BF00876395

Tape, C., Liu, Q., Maggi, A., and Tromp, J., 2009, Adjoint tomography of the southern California crust: *Science*, **325**(5943), 988–992. doi:10.1126/science.1175298

Tarantola, A., 1984, Inversion of seismic reflection data in the acoustic approximation: *Geophysics*, **49**(8), 1259–1266. doi:10.1190/1.1441754

Thurber, C. H., 1983, Earthquake locations and three-dimensional crustal structure in the Coyote Lake area, central California: *Journal of Geophysical Research. Solid Earth*, **88**(no. B10), 8226–8236. doi:10.1029/JB088iB10p08226

Thurber, C. H., 1992, Hypocenter-velocity structure coupling in local earthquake tomography: *Physics of the Earth and Planetary Interiors*, **75**(1–3), 55–62. doi:10.1016/0031-9201(92)90117-E

Waldhauser, F., and Ellsworth, W. L., 2000, A double-difference earthquake location algorithm: Method and application to the northern Hayward Fault, California: *Bulletin of the Seismological Society of America*, **90**(6), 1353–1368. doi:10.1785/0120000006

Warpinski, N. R., 2013, Understanding hydraulic fracture growth, effectiveness, and safety through microseismic monitoring: ISRM International Conference for Effective and Sustainable Hydraulic Fracturing, International Society for Rock Mechanics, ISRM-ICHF-2013-047.

Warpinski, N., Branagan, P., Peterson, R., Wolhart, S., and Uhl, J., 1998, Mapping hydraulic fracture growth and geometry using microseismic events detected by a wireline retrievable accelerometer array: SPE Gas Technology Symposium, Society of Petroleum Engineers, SPE-40014-MS.

Warpinski, N. R., Sullivan, R. B., Uhl, J. E., Waltman, C. K., and Machovoe, S. R., 2003, Improved microseismic fracture mapping using perforation timing measurements for velocity calibration: *Society of Petroleum Engineers Journal*, **10**, 14–23.

Witten, B., and Shragge, J., 2015, Extended imaging conditions for passive seismic data: *Geophysics*, **80**(6), WC61–WC72. doi:10.1190/geo2015-0046.1

Witten, B., and Shragge, J., 2017*a*, Image-domain velocity inversion and event location for microseismic monitoring: *Geophysics*, **82**(5), KS71–KS83. doi:10.1190/geo2016-0561.1
Witten, B., and Shragge, J., 2017*b*, Microseismic image-domain velocity inversion: Marcellus Shale case study: *Geophysics*, **82**(6), KS99–KS112. doi:10.1190/geo2017-0263.1
Zoback, M., 2007, *Reservoir geomechanics*: Cambridge University Press.
Zoback, M. D., and Gorelick, S. M., 2012, Earthquake triggering and large-scale geologic storage of carbon dioxide: *Proceedings of the National Academy of Sciences of the United States of America*, **109**(26), 10164–10168. doi:10.1073/pnas.1202473109

Ben Witten recently completed his PhD in geophysics at the University of Western Australia. He also holds a BS in applied mathematics from Columbia University and an MS in geophysics from Stanford University. Prior to commencing his PhD, he worked at Spectraseis performing R&D and processing of micro-seismic monitoring data.